Materials Today Advances 21 (2024) 100477

Contents lists available at ScienceDirect

Materials Today Advances

journal homepage: www.journals.elsevier.com/materials-today-advances/

Copper–zinc oxide heterostructure photocathodes for hydrogen and methanol production

Tomasz Baran [a,b,*], Szymon Wojtyła [b], Marco Scavini [c], Francesco Carlà [d], Edmund Welter [e], Roberto Comparelli [f], Angela Dibenedetto [g,h,**], Michele Aresta [a]

[a] Innovative Catalysis for Carbon Recycling-IC^{2}R, via Camillo Rosalba 49, 70124, Bari, Italy
[b] SajTom Light Future Ltd, Wężerów 37/1, 32-090, Wężerów, Poland
[c] Università degli Studi di Milano, Dipartimento di Chimica, via Golgi 19, 20133, Milano, Italy
[d] Diamond Light Source Ltd, Didcot, Oxon, OX11 0DE, UK
[e] Deutsches Elektronen-Synchrotron DESY, Germany
[f] CNR-IPCF, Istituto per i Processi Chimico-Fisici, S.S. Bari, c/o Dipartimento di Chimica, Via Orabona 4, 70126, Bari, Italy
[g] Department of Chemistry, University of Bari Aldo Moro, Bari, 70125, Italy
[h] CIRCC, via Celso Ulpiani 27, Bari, 70126, Italy

ARTICLE INFO

Keywords:
Photoelectrochemistry-PEC
CO_2 PEC reduction
PEC water splitting
Copper oxide
Zinc oxide
Hydrogen evolution
Methanol production from CO_2 and water

ABSTRACT

Low activity and a short lifetime are the main weaknesses of photocatalysts. The photoactivity of copper oxide, which is known as one of the most promising materials for H_2 evolution and CO_2 reduction, can be improved by coupling with other semiconductors. This effect is based on a mutual charge transfer. The photocathode developed in this work, based on a CuO–ZnO composite with mutual self-doping, exhibits attractive photoelectrochemical properties, in particular a high density of generated photocurrent lasting for 24 h. Under visible light irradiation, the composite produces water-splitting, while in the presence of carbon dioxide it is able to perform CO_2 reduction to methanol with good selectivity coupled to water oxidation. The high activity of the CuO-based cathode is due to the presence of zinc oxide, which is progressively leached, causing a slow decrease of the photoactivity of the material.

1. Introduction

The use of sunlight to convert carbon dioxide and/or water into fuels might contribute in moving away from fossil-carbon with the double benefit of saving fossil resources and mitigating the CO_2 atmospheric level [1–4]. In this aspect, photoelectrochemical (PEC) and photocatalytic (PC) water splitting coupled to CO_2 reduction appear a strategic approaches investigated with growing interest in recent years. The production of so called Solar Fuels is relevant to carbon-recycling and sustainable development [5–9]. Despite the considerable efforts, the characterization of photo(electro)catalytic materials lacks completeness and the used photocatalysts do not fulfill the requirements of high efficiency, long-term stability and low cost, while reasons for their deactivation are not always clarified. In fact, semiconductors are usually characterized by sluggish photoelectrochemical (photocatalytic) reaction kinetics, thus limiting the overall system efficiency. To overcome this limitation, the coupling of electrocatalysts and semiconductor surfaces has been attempted. The most active materials are semiconductors coupled to noble metal electrocatalysts such as platinum, ruthenium, gold, iridium oxide, or palladium [13,18] which afford a better light absorption due to a surface plasmon resonance and an improved activity because noble metals can work as electron traps and active reaction sites, in Hydrogen Evolving Reaction (HER), CO_2 reduction (CO_2R) or Oxygen Evolving Reaction (OER) [10]. The development of cheap and efficient photocathodes is still a huge challenge and thus, in order to implement PEC water splitting or carbon dioxide reduction at an industrial scale, new stable, cheap materials should be developed based on abundant elements able to efficiently and selectively drive the HER or CO_2R coupled to OER. Consequently, it is important to develop novel cheap PEC materials that are fully characterized, generate

* Corresponding author. Innovative Catalysis for Carbon Recycling-IC^{2}R, via Camillo Rosalba 49, 70124, Bari, Italy.
** Corresponding author. Department of Chemistry, University of Bari "Aldo Moro", Bari, 70125, Italy; CIRCC - University of Bari, via Celso Ulpiani 27, Bari, 70126, Italy
E-mail addresses: tommaso.baran@gmail.com (T. Baran), angela.dibenedetto@uniba.it (A. Dibenedetto).

https://doi.org/10.1016/j.mtadv.2024.100477
Received 6 November 2023; Received in revised form 5 February 2024; Accepted 17 February 2024
Available online 6 March 2024

a high photocurrent density and provide a large photovoltage and to understand the reasons for their deactivation with time.

Copper oxide (CuO) is an example of a material for PEC water splitting or CO_2 reduction [11–16]. It is a *p*-type semiconductor, abundant and cheap, that can produce high photocurrents, has the correct band gap energy for visible light utilization and the potential for both HER and OER. Due to such properties, CuO has been intensively studied for solar light induced H_2-production [13,17,18]. On the other hand, the photo-stability of copper oxide is not high enough for long term application [18]. As a consequence of photocorrosion, a part of measured photocurrent may not be relevant to H_2-generation. For making its use as a H_2-evolution photocathode practical, the protection of CuO has been attempted through the formation of oxide-composites. For example, the CuO/$CuFe_2O_4$ core−shell structure affords a 100% faradaic efficiency for hydrogen evolution [19]. Recently, we have demonstrated the improved activity and stability of Cu_2O/CuO composites, in which mutual transfer of photogenerated charges occurs between CuO and Cu_2O [11,20].

Literature reports few examples of copper-zinc composites for HER or CO_2 reduction, such as a core shell CuO/ZnO [21–24] and ZnO/-Cu_2O–CuO [25], a simple mixed oxide ZnO–CuO [26–29], and CuO doped with Zn ions [30]. Similarly, we have recently described the improved photocatalytic activity of copper-zinc nanoflowers toward hydrogen evolution [31]. It has been reported, that coupling CuO with ZnO produces effects such as significant improvement in the photocathodic current [23], improved selectivity of CO_2 reduction to C_2 products [22], or enhanced hydrogen evolution [23,28]. Such heterostructures can prolong the electron-hole pair lifetime and prevent unfavorable recombination of photogenerated carriers because of the well-matched energy-band positions, which facilitate reverse transfer of positive and negative charges across the *p-n* interface [23,24].

The main objective of the present work was to study a low-cost approach based on charge transition for improving the activity of a copper oxide-based photocathode. The novel aspect of this work is the simple methodology used for the preparation of materials that does not involve any organic precursors, stabilizers, or surfactants so to avoid that residual organics during the application of the catalyst may be converted into molecules that can eventually be generated from CO_2, leading to a false positive result [32]. Copper – zinc materials analogous to our photocatalysts were usually prepared in literature papers by using organic compounds such as EDTA, acetates, alcohols, and other organic solvents [21,26–29,31] that we have avoided. The goal of this paper has been achieved by coupling CuO with ZnO in a mutual-self-doped composite, even easily prepared by drop-casting of the mixture of Cu^{2+} and Zn^{2+} onto a conductive support, followed by annealing in air. This approach has allowed us to obtain a much better contact between CuO and ZnO in comparison with mixed oxides or doped materials, because the lattices of both oxides contain the host cation. The photo-electrocatalytic activity of the copper-zinc cathode has been studied towards the dual application under visible light: reduction of water to H_2 or CO_2 to methanol (with water oxidation). We have found, that ZnO in the host CuO lattice increases and stabilizes the photoactivity of the latter that remains active for as long as 24 h continued operation.

2. Experimental

2.1. Synthesis of materials

The CuO–ZnO electrode was prepared by a simple drop-casting method followed by annealing in air. Therefore, 0.05 mol of Zn $(NO_3)_2{\cdot}6H_2O$ (Alfa Aesar) were dissolved in 0.01 M nitric acid (1 mL). The so obtained solution was dropped to $Cu(NO_3)_2$ (Sigma-Aldrich) aqueous solution (0.05 mol, 4 mL). The resulting mixture was stirred for 3 h. Fluorine-doped tin oxide (FTO) coated glass (Sigma Aldrich, ~8 Ω/sq) substrates (1 cm × 2 cm) was cleaned by taking it through RCA treatment (FTO in 1:1:5 vol ratio of NH_3, 30% H_2O_2 and H_2O was heated at 70 °C for 15 min, thereafter it was rinsed with double deionized-DI water 3–4 times under ultrasound). The precursor Cu + Zn aqueous (0.25 mL/cm^2) was drop-cast onto FTO substrate lying flat at warm plate (40 °C). After drop-casting the electrode was left for *ca.* 20 min to complete the evaporation of the solvent. Subsequently, it was heated to 450 °C (unless otherwise stated) in a muffle furnace with a ramp rate of 10 °C/min and held for 2 h. To increase the electrode-thickness, the drop-casting procedure was repeated up to drop-cast 4 layers. Such electrodes will be denoted as "CuO–ZnO".

2.2. Characterization of the materials

UV–Vis Diffuse Reflectance Spectra (DRS) were recorded using a UV-2600 spectrophotometer (Shimadzu) equipped with an integrating sphere (ISR-2600Plus). Barium sulfate was used as a reference material. The spectra of CuO–ZnO photocathode were obtained directly from the electrode.

XRPD (X-ray powder diffraction) data were collected at the ID03 beamline of the ESRF (European Synchrotron Radiation Facility in Grenoble) using a six-circles diffractometer operating in grazing incidence geometry. Data were collected with a Maxipix detector [32] using an incident energy of 24 keV (equivalent to 0.5166 Å). The data were collected using an 'in-plane' scan geometry with the detector positioned at 0.4° above the sample horizon, the images were processed with the BINoculars software [33] in order to obtain Intensity/2θ curves. During the experiment the samples were maintained under a nitrogen atmosphere and a set of slits positioned in the proximity of the samples allowed to cut the scattered intensity from the entrance and exit windows of the sample environment. The samples were measured using various incident angles (0.1°, 0.2°, 0.5° and 1°). The comparison between the different data sets allowed the identification of the crystallographic structures present in the film and the signal of the SnO_2 phase (FTO glass) generated by the substrate. Noteworthy, as the penetration depth of the beam below the sample surface is depending on the angle of incidence (higher angles implies deeper penetration) it is possible to decouple the contributions of the film and the substrate by confrontation of the diffraction patterns obtained in different experimental conditions.

Elemental analysis was performed by using Energy-dispersive X-ray spectrometry (EDX) using a EDX-7000P spectrometer (*Shimadzu*).

Field emission scanning electron microscopy (FE-SEM) was performed by using a Zeiss Sigma microscope operating in the range 0.5–20 kV and equipped with an in-lens secondary electron detector and an INCA Energy Dispersive Spectroscopy (EDS) detector. Samples were mounted onto stainless-steel sample holders by using double-sided carbon tape and grounded by silver paste.

XAS measurements were performed at the Deutsches Elektronen-Synchrotron. Samples were measured in total fluorescence yield mode using a Canberra PIPS diode detector, with the coated side facing the incoming X-ray beam. Cu K-edge and Zn K-edge measurements were performed. The parameters of measurements were: scan range: 150 eV to +1000 eV around respective edge; time per single scan equal to 180 s; beam-size on sample equal to 0.2 * 1.2 mm^2 (v*h); double crystal monochromator: Si 111 for Ni, Cu, Zn K-edge always detuned to 85 % of maximum intensity for additional higher harm-suppression. Higher harmonics suppressing mirrors: plane, Si/Si 2 mrad.

2.3. Electrochemical characterization

A three-electrode quartz cell was used in photoelectrochemical measurements for applying potentials profile at the photocathode equivalent to linear voltammetry or constant potential. Photoelectrochemical measurements were controlled by BioLogic SP-150 potentiostat. CuO–ZnO cathodes were the working electrode and a silver chloride electrode (Ag–AgCl) and a platinum spiral were used as the reference and the counter electrodes, respectively. The scan rate was 10

mV/s. A LED (λ = 400 nm) was used as light source (unless otherwise stated). The illumination was from the frontside. The electrolyte was bubbled with nitrogen prior to each measurement and a N_2-blanket was kept on top of the solution during all experiments. Concentration, composition and pH of the electrolytes are specified per each experiment. Electrochemical potentials were converted to the reversible hydrogen electrode (RHE) scale. The hydrogen product from the head space above the reaction solution was analyzed by gas chromatography (Nexis GC-2030, *Shimadzu*) with thermal conductivity detector (TCD) operating at 250 °C and a current of 35 mA. Molecular sieve 5A capillary column was used for the separation. The carrier gas was high purity argon. Tests towards CO_2 reduction was performed in 0.5 M sodium hydrogencarbonate, that act as an electrolyte and CO_2 source. Electrolyte was deoxygenated prior to the test. The 3-electrode setup was prepared as described above. Tests were performed as a chronoamperometric run under chopped light (3 s light and 4 s dark), with the electrode biased at 0.55 V *vs* RHE. The reaction progress was monitored using GC-BID analysis, injecting the sample in a headspace mode.

Electrochemical impedance spectroscopy (EIS) measurements were performed in the deoxygenated electrolyte (by means of N_2 bubbling) - 1 M NaOH, pH = 14. Impedance spectra were recorded at a constant potential in the frequency range 100 kHz to 100 mHz using a SP-150 BioLogic analyzer. The potential was stepped by 0.05 V with a waiting time of 200 s before the next spectrum was recorded. The equivalent circuit used to fit the impedance spectra contains the solution resistance, the polarization resistance and the constant phase element (CPE) associated to the space charge capacitance, C_{SC} (*vide infra*). The impedance of the CPE, $Z_{CPE,}$ is given by

$$Z_{CPE} = \frac{1}{Q(j\omega)^{\alpha}} \quad (1)$$

where ω is the frequency and α equals unity for an ideal capacitor. When α equals 1, the CPE simplifies to a capacitor, while when α is 0, the CPE represents a pure resistor, and when α equals −1, the CPE behaves as a pure inductor. The CPE is a flexible circuit element, but its physical meaning is still controversial [34]. Since in the present case α was close to 1, we assigned the numerical value of Q to the $C_{SC.}$

Spectroelectrochemical measurements were carried out in a three-electrode system with Drop-Sens 110 screen-printed carbon-electrode (carbon and silver) as a reference and counter electrode, while CuO–ZnO deposited onto FTO was used as a working electrode (the electrodes were at least partially transparent). The electrodes were placed in a quartz cuvette filled with 0.1 M phosphate buffer (pH = 7). Oxygen was thoroughly removed from the solution by bubbling pure nitrogen before experiments. The cuvette was placed inside the spectrophotometer (UV-2600 Shimadzu) chamber with working electrode facing the light source (Fig. S1). The electrode potential was controlled by a potentiostat (Bio-Logic, SP-150). The applied potential was lowered every10 min by 50 mV. Scan rate was 2 mV/s. Changes in the absorbance were observed at 370 nm.

3. Results

3.1. Structure, elemental analysis and morphology of the cathodes

CuO–ZnO cathodes were prepared by a simple drop-casting of a solution of zinc and copper salts. The chemical composition and structure of the as-prepared photocathode were investigated by using EDX and synchrotron XRPD techniques. CuO–ZnO is composed only of copper, zinc and oxygen as demonstrated by EDX spectrometry (Fig. S2). XRPD measurements carried out at 0.1° angle (Fig. 1) showed three phases present: the Tenorite *C*2/*c* phase of CuO [wf = 0.155(3)], the hexagonal Zincite $P6_3mc$ phase of ZnO [wf = 0.227(2)] and the tetragonal $P4_2/mnm$ phase of SnO_2 (fluorine doped tin oxide glass support) [weight fraction wf = 0.618(2)]. With increasing the incident angle, the contribution of tin oxide phase (FTO support) increased (Fig. S3). The refined parameters for the pattern collected at the lowest incident angle (0.1) on the CuO–ZnO system are summarized in Table 1, while all patterns are in Table S1 in SI. In Fig. 1 B a detail of the experimental patterns is shown. Experimental data (crosses) are displayed together with the calculated contributions of the SnO_2, CuO and of the ZnO

Table 1
Structural parameters extracted from Rietveld refinement of synchrotron XRPD patterns for CuO–ZnO. Data for SnO_2 are not shown. U = 0.0202(3) $Å^2$, Rp 0.0518.

	0.1°	Literature
a CuO/Å	4.739(1)	4.653(10) [37]
b CuO/Å	3.405(1)	3.41(1) [37]
c CuO/Å	5.137(2)	5.108(10) [37]
β CuO/°	99.87(2)	99.48(33) [37]
a ZnO/Å	3.2591(3)	3.2417 [38]
c ZnO/Å	5.2207(8)	5.1876 [38]

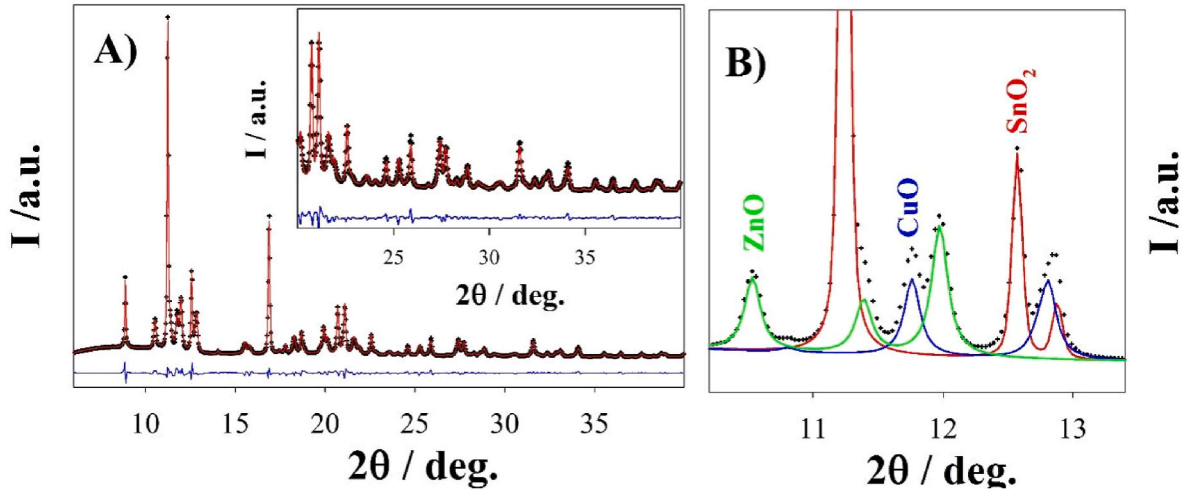

Fig. 1. (**A**) Experimental XRPD pattern (black lines) of CuO–ZnO photocathode collected at 0.1° together with the best fit (red trace) and the residuals (blue trace). The inset highlights the high 2θ range. (**B**) Detail of the experimental data (black lines) together with the calculated contributions of the SnO_2, CuO and ZnO phases shown as red, blue and green lines, respectively. (For interpretation of the references to color in this figure legend, the reader is referred to the Web version of this article.)

phases, the red, blue and green lines, respectively. The diffraction peaks of both CuO and ZnO phases are well identified. Indexed patterns are shown in Fig. S4 in SI.

XRPD results show that CuO and ZnO form each a separated phase. As shown in Table 1 and Table S1, their cell constants are larger with respect to the single oxide literature data. The presence of zinc in a CuO cell leads to its enlargement, due to the larger ionic radius of Zn^{2+}(IV) = 0.60 Å with respect to Cu^{2+}(IV) = 0.57 Å [35]. As to the ZnO phase, the effect should be the opposite because the ionic radius of copper is smaller than that of zinc. As a matter of fact, the observed enlargement of the cell parameters matches literature data [36] and is explained as Cu doping of ZnO induces an expansion of the ZnO thin film parameters due to the increased crystallinity of ZnO. K. Joshi et al. [36] have explained such effect on the basis of the removal of external stress arising from the lattice mismatch between substrate and film. Systematic effects (e.g. photon energy offsets) can be safely excluded since SnO_2 cell constants are indeed shrunk with respect to literature references (see Table S1). SnO_2 can be, thus, considered as a reference material that allows to distinguish systematic effects from real changes that occur in material.

SEM micrographs given in Fig. 2 shows that the obtained material is composed micrometric aggregates of nearly spherical nanoparticles in the range of several nanometers (20–200 nm) distributed over the FTO surface. The EDS mapping highlights the presence of copper mainly in the flower-like aggregates, while Zn is distributed on the whole surface of FTO although a higher density of yellow spots can be observed on the flower-like aggregates (Fig. 2C and D,E). Thy typical mechanism of flower-like materials formation includes a few steps: nucleation, self-aggregation, Ostwald ripening and dissolution and recrystallization [39,40]. We assume that our flower-like materials are formed according to such mechanism.

3.2. Optical absorption properties and a band structure

The most important parameters of a semiconducting material, determining its utility in photoelectrochemical or photocatalytic processes are the band gap energy and the potential of conduction and valence bands. The light absorption is the first stage of the photocatalytic and photoelectrochemical water splitting. Before a photoactive material can generate an electron-hole pairs, it must efficiently catch the light energy. To assess the light absorption of the CuO–ZnO photocathode and materials, we performed a UV–Vis analysis with an integrating sphere. The material absorbs light in a broad wavelength range with maximum in UV. The reflectance spectra for CuO–ZnO films prepared directly on FTO glass substrates using various numbers of deposited layers are shown in Fig. 3. The reflectance (%) decreases with increasing the number of layers, thus the amount of light absorbed by the photoelectrode is higher in case of larger amount of material deposited on the FTO, in accordance with Beer–Lambert law. Typical DRS measurements have been carried out using a 1–2 mm thick layers materials deposited on FTO glass. Reflectance spectra of the photocathodes have been converted to Kubelka-Munk function (KM), defined as in Eq. (1):

$$F_{KM}(R_\infty) = \frac{(1-R_\infty)^2}{2R_\infty} = \frac{\alpha(h\nu)}{S} \quad (1)$$

where R∞ is the diffuse reflectance referred to a layer of infinite thickness, S the scattering coefficient and α(hν) the absorption coefficient. Kubelka-Munk function was used to determine the band gap energy of semiconductor from Tauc plot (Fig. S5). Both direct and indirect bandgap Tauc plots have been created. However, only direct plot shows a straight line with a sharp onset. Regardless of the number of layers the band gap energy of CuO–ZnO is 2.43 eV (see Fig. S5).

Mott-Schottky measurements (from EIS) were performed to estimate

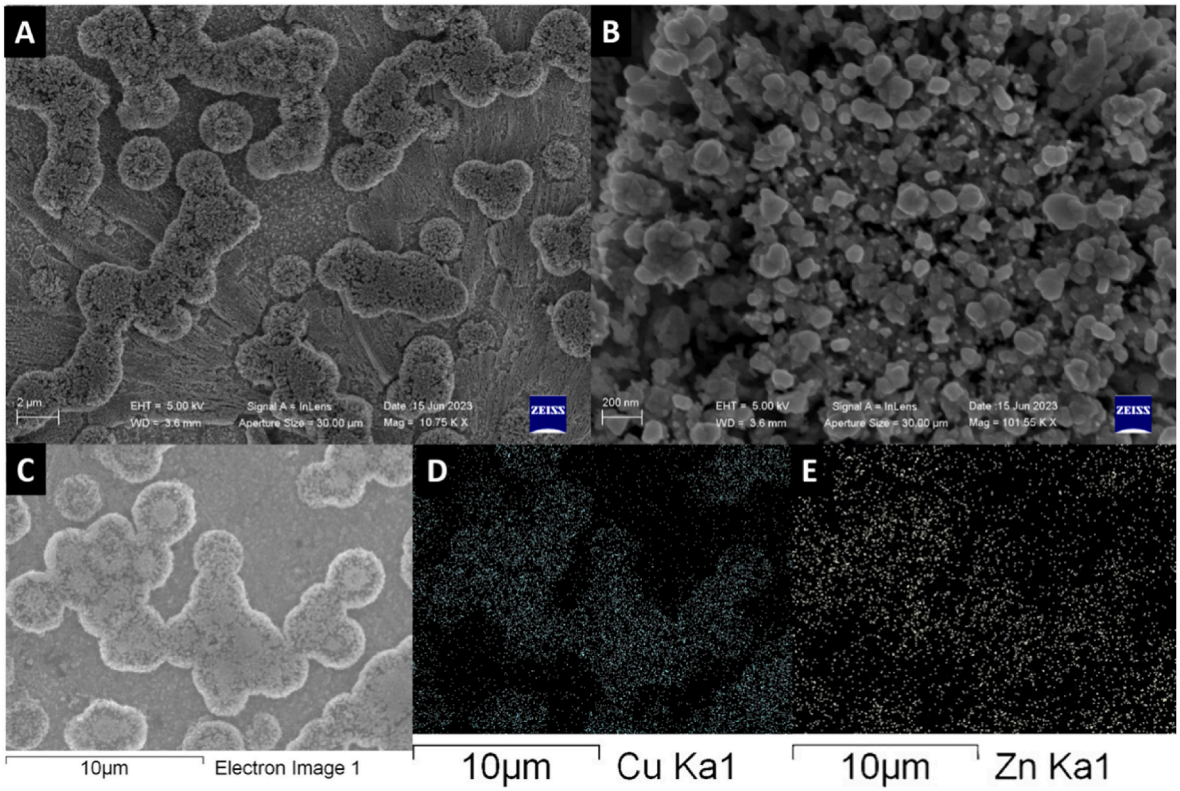

Fig. 2. SEM micrographs (**A,B**) and EDS mapping (**C,D,E**) of CuO–ZnO photocathode. (A,B) Secondary electron images recorded at 10 kX and 100 kX, respectively. (C) Electron image and false color spatial distribution of Cu (D) and Zn (E). (For interpretation of the references to color in this figure legend, the reader is referred to the Web version of this article.)

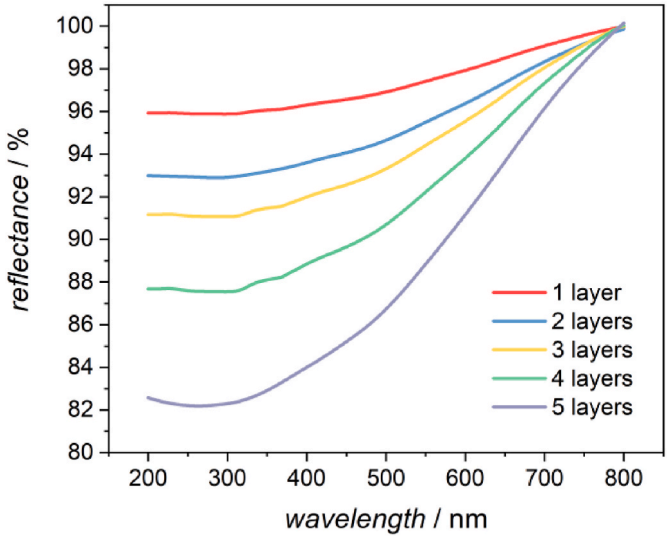

Fig. 3. The normalized diffuse reflectance spectra and the influence of the number of layers on the spectrum of CuO–ZnO.

the location of the Fermi level. To this end, the space charge capacitance (C_{sc}) of the CuO–ZnO/solution interface was measured in a selected range of frequencies and various applied potentials at pH 14. The results are shown in Fig. 4 as Nyquist curves and Mott-Schottky plot, where the linear portion is described by Eq. (2):

$$1 / C_{SC}^2 = 2 / e\varepsilon\varepsilon_0 N(E - E_{FB} - kt / e) \quad (2)$$

where ε is the dielectric constant of the sample, ε_0 is the vacuum permittivity, e is the elementary charge, N is the acceptors concentration (for a p-type semiconductor), E_{FB} is the flat band potential, k is the Boltzmann constant, T the temperature [41]. The capacitances of the electrochemical double-layer in the case of electrodes polarized with various potentials were calculated using the equivalent circuit shown in Fig. S6 and used to obtain the Mott-Schottky plot. The Mott-Schottky plot of CuO–ZnO exhibits a negative slope, indicating that the material has a *p*-type semiconducting character – the same as CuO, different than ZnO. The straight-line extrapolation leads to 1.20 V vs RHE.

3.3. Photoelectrochemical activity

The performance of a photoelectrochemical material can be judged by the photocurrent density. Photocathodes were tested in a variety of electrochemical and photoelectrochemical measurements, including cyclic and linear sweep voltammetry, electrochemical impedance spectroscopy (EIS) as well as incident photon to current efficiency (IPCE) measurements, and spectro-electrochemical experiments. Fig. 5A shows chopped (light 3s/dark 4s) linear sweep voltammetry results for CuO–ZnO photocathodes under nitrogen bubbling. Nitrogen was used to purge dissolved oxygen and suppress the O_2 reduction reaction, which may affect the observed photocurrents. Under irradiation, materials showed cathodic photocurrents in a broad potential range. At 0.35 V *vs*. RHE the CuO–ZnO photocathode generates a photocurrent density of ~1.5 mA cm^{-2}. However, upon potential higher than 0.84 V *vs* RHE, anodic photocurrents (up to 150 μA cm^{-2}) were observed. The potential induced photocurrent switching effect can be most likely explained in terms of the presence of the two phases, namely Zn@CuO and Cu@ZnO which can be responsible of the photocurrent under cathodic and anodic conditions, respectively. It is well known, that *n*-type semiconductors generate anodic photocurrents, while *p*-type produce cathodic photocurrents [42]. A noticeable dark current, most likely from corrosion, was observed at negative potentials.

Data shown in Fig. 5A, demonstrate the huge influence of the number of layers on photocurrent density in the range from 2 to 4 layers. Photoelectrodes composed of 5 or 6 layers showed a noticeable lower photocurrent density in comparison with 4 layers (Fig. S7). Such behavior can be explained assuming that increasing the thickness of photocathode, photons cannot reach deeper layers of photocathodes. On the other hand, a thicker photocathode may absorb more light, but in the thicker electrode the migration of photogenerated charges to the FTO support is more difficult and takes a longer time [43]. Since calcination temperatures can affect the structural properties of photocatalyst, the photoelectrochemical features of CuO–ZnO at different calcination temperatures were investigated. Fig. 5B shows the comparison of photocurrents generated by electrodes calcined at 450 °C and 550 °C, depending on the number of layers. According to these results, the calcination at 450 °C produces significantly more active photocathodes. The differences in photoactivity can be explained on the basis of structural changes occurring at higher calcination temperature, that may affect co-doping CuO/ZnO, however, these changes are still under study and will be matter of a forthcoming paper.

Fig. 5C shows the chopped (light/dark) linear sweep voltammetry

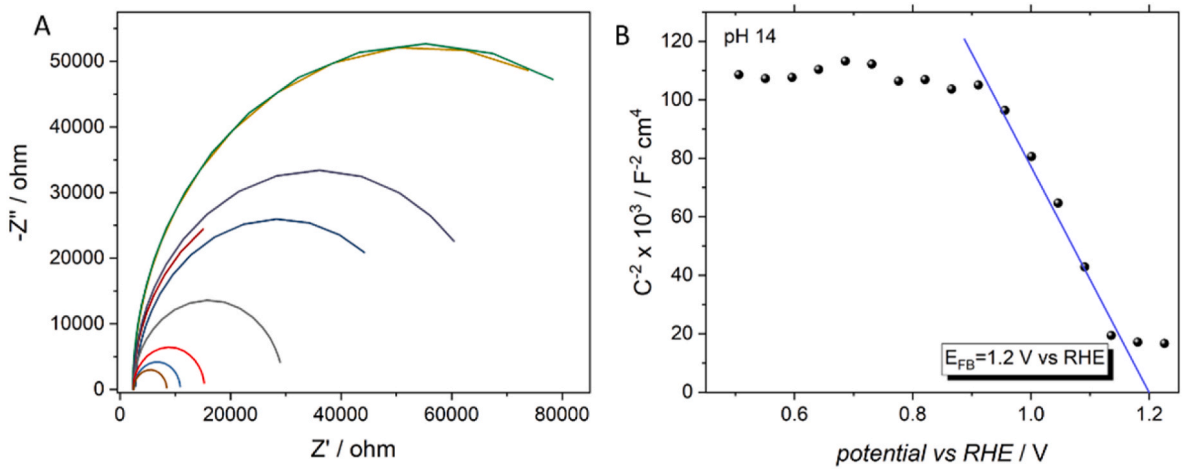

Fig. 4. Electrochemical impedance measurements carried out for CuO–ZnO prepared at 450 °C. A - Nyquist plots measured (frequency sweep mode) in the dark at various potentials (each line represents one potential; not all curves are shown to keep the chart clear) in the range of 0.51–1.23 V versus RHE. B - Mott-Schottky plot for CuO–ZnO at pH 14. E_{FB} calculated from linear fitting (blue curve in fig B). (For interpretation of the references to color in this figure legend, the reader is referred to the Web version of this article.)

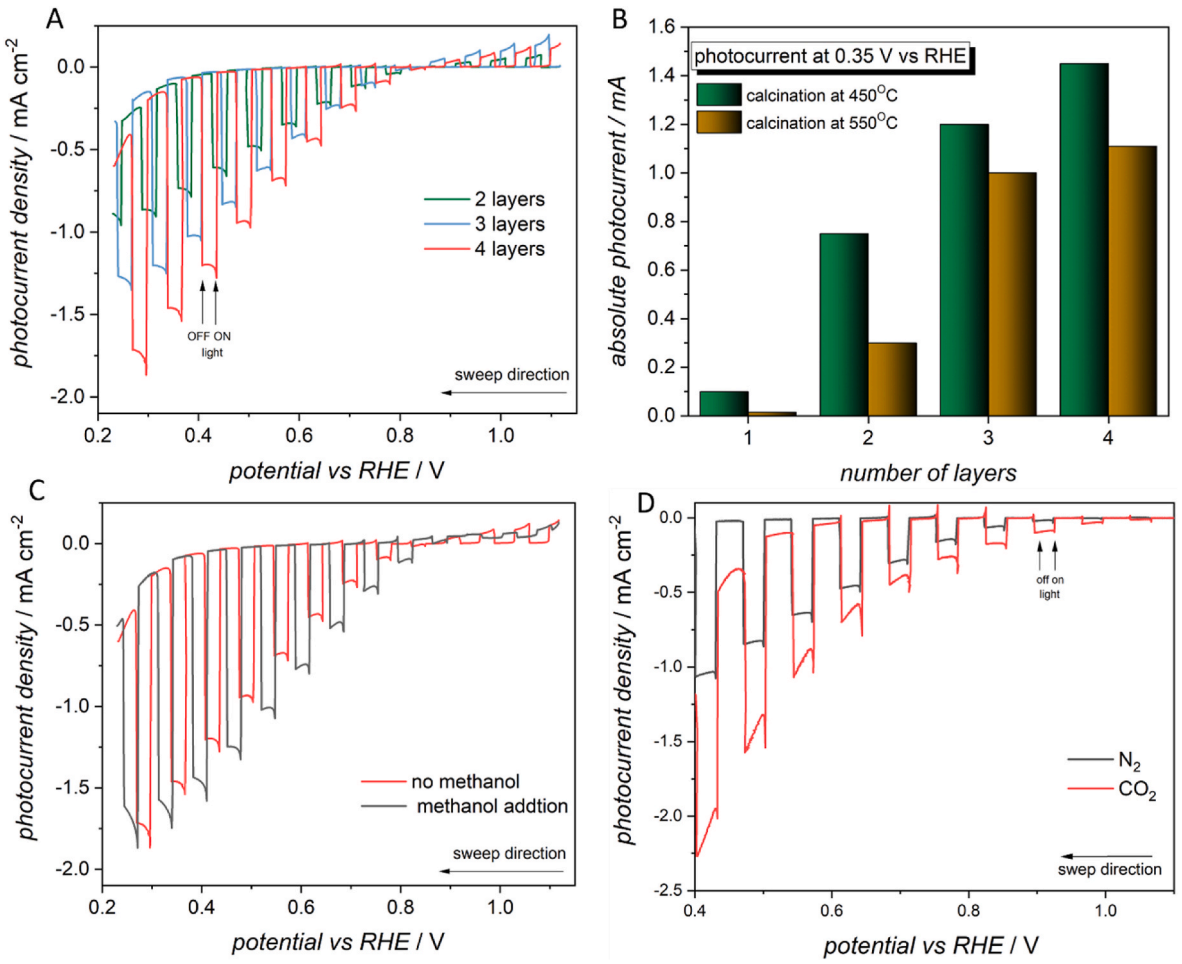

Fig. 5. Chopped (light/dark) linear sweep voltammetry measurements for CuO–ZnO photocathodes composed of 2, 3 and 4 layers of deposited material. Scans performed in 1 M NaOH (pH 14) with nitrogen bubbling (**A**). Comparison of the effect of the calcination temperature and the number of layers (**B**). Chopped (light/dark) linear sweep voltammetry scans for CuO–ZnO (4 layers) in 1 M NaOH with or without 5 vol% addition of methanol (**C**). Chopped (light/dark) linear sweep voltammetry scans for CuO–ZnO (4 layers) in 1 M NaOH in N_2 or CO_2 atmosphere (**D**).

scans for CuO–ZnO photocathodes with nitrogen purging (**A**) and with methanol added as a hole scavenger (**C**). CuO–ZnO photocathode shows miniscule cathodic transient spikes, which can be caused by surface recombination or back reaction of the photogenerated species. According to the literature, it can presumably result from a high density of charge surface traps [44]. Noteworthy, the addition of methanol only faintly increases the density of photocurrents suggesting that the potential of photogenerated holes is such to effectively oxidize water, making superfluous the addition of sacrificial donors such as methanol.

Photocurrent measurement in an atmosphere of carbon dioxide (Fig. 5D) shows increased density of generated photocurrent in the whole potential range. At the same time, the dark current also shows higher density but only for the lowest potentials. Increased photocurrent density suggests that the photogenerated electron from conduction band of irradiated materials can participate in cathodic reaction, namely the reduction of carbon dioxide. In this sense, CO_2 can serve as an acceptor of electron in competition with water molecule.

The photocurrent density strongly depends on the wavelength of incident light and the dependence correlates with the UV–Vis absorption spectrum of materials. The IPCE of CuO–ZnO photocathodes was measured at 0.4 V *vs* RHE (chronoamperometric measurements for each wavelength) at pH = 7, using equation (3)

$$IPCE(\%) = \left(\frac{1240 \bullet I_{ph}}{J \bullet \lambda}\right) \bullet 100. \quad (3)$$

where λ is the wavelength of the incident light, I_{ph} and J are the measured photocurrent density and the measured irradiance at the selected wavelength, respectively. As shown in Fig. 6, IPCE exceeds 25% for ultraviolet and reaches a value of up to 20% for visible light, a much higher value than that found for the mixed oxide ZnO/CuO, that showed an IPCE up to 12% [29,45,46]. Such features clearly shows that the two materials (the literature and that described in this work) have a different structure.

Aside from the solar-to-hydrogen efficiency, the most important feature of a water splitting system is the life span of the PEC devices. The long-term stability at pH = 14 was investigated under chopped light (light/dark frequency 0.12 Hz) at a constant potential of 0.4 V *vs.* RHE with nitrogen atmosphere. As demonstrated in Fig. 7, the efficiency of light conversion slightly decreases during the first 3 h and then the material reaches a nearly stationary condition since the photocurrent density does not change significantly with time, up to 24 h generating relatively high photocurrents, approximately 0.65 mA. This represents a large improvement with respect to CuO–ZnO systems described in the literature that are able to generate photocurrents in the range from minutes up to 1 hour [29,47,48].

In addition to having appropriate potentials of conduction and valence bands, a photocathode should also possess a large internal photovoltage in order to evolve hydrogen at positive potentials (higher than 0 V). Photovoltage can be understood as a thermodynamic driving force of the photoelectrode [49]. The differences between open circuit

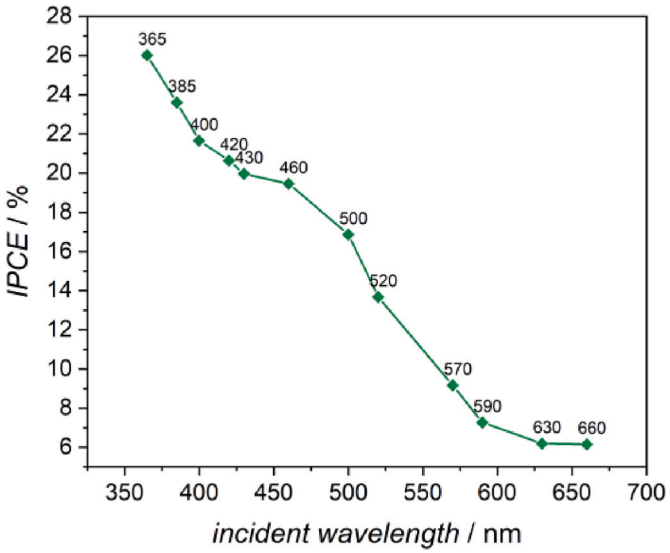

Fig. 6. IPCE spectra for CuO–ZnO photocathodes (4 layers, 450 °C). The chronoamperometric measurements were performed at a potential of 0.4 V *vs.* RHE in a 1 M NaOH with nitrogen bubbling. The illumination was from the backside.

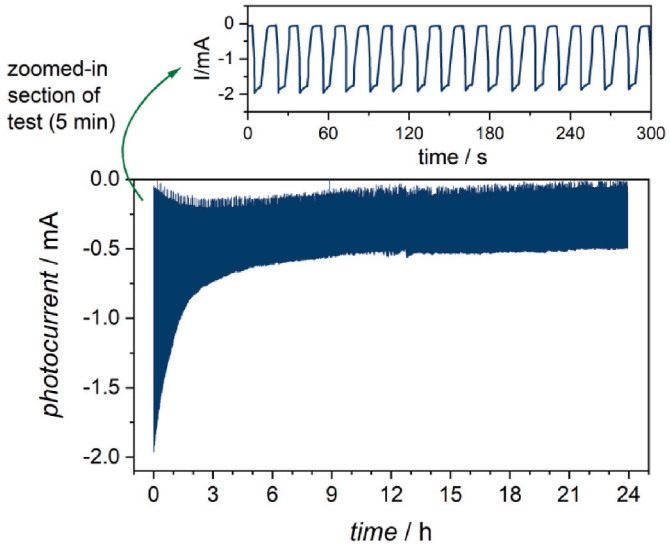

Fig. 7. Stability test at 0.4 V *vs.* RHE in 1 M NaOH (pH = 14) under chopped illumination with LED (λ = 400 nm). Upper graph: zoom on initial time scale (300 s).

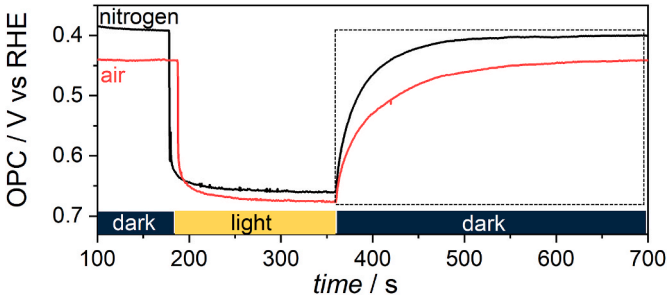

Fig. 8. Open-circuit potential (OCP) measurements in the dark and light for a CuO–ZnO photocathode (4 layers, 450 °C) in air or with N_2 bubbling.

potential in the dark and under illumination (ΔOCP) can estimate the photovoltage and reflect the change in the Fermi level of the majority carriers although it is affected by the redox properties of the solution. Fig. 8 shows the results of OCP measurement in dark-illumination-dark sequence. In the dark, noticeable differences between the system in the air or nitrogen atmosphere were observed. Under light, OCP increases due to the shift in the Fermi level. If the rate of electron-hole pairs generation under light is faster than the rate of intrinsic recombination, the bands can completely flatten [49]. The change of open circuit potential reflects the amount of band bending in the material occurring in dark. The ΔOCP was 0.26 V when bubbling N_2 and 0.23 V in presence of oxygen. The difference between the two conditions is very small. This suggests that the bands flattening is not dependent on the presence of oxygen in the electrolyte.

3.4. Photoelectrochemical activity towards H_2 and CH_3OH formation

The photoactivity of material towards H_2O reduction to H_2 and CO_2 reduction to CH_3OH was studied in photoelectrochemical conditions. Biased working electrodes immersed in deoxygenated electrolyte showed the ability to evolve the hydrogen or, in the presence of CO_2, to methanol formation. The photoactivity of CuO–ZnO towards H_2 evolution was determined using gas chromatography measurements. PEC tests were performed in a classic electrochemical cell, in which oxygen was excluded at the maximum extent. However, obtained data (Fig. 9A) clearly point at H_2 formation, at a rate equal to *ca.* 80 μmol $g_{cat}^{-1}h^{-1}$. The calibration curve is reported in Fig. 9A - inset).

Taking into account the increased photocurrent density observed in the presence of carbon dioxide (Fig. 5D) the PEC test of CO_2 reduction was performed. Density of measured photocurrents under chopped light (Fig. 9B) decreased during 30 min test under bias at 0.55 V *vs* RHE. GC analyses performed on samples taken at 10 min interval clearly proved the formation of methanol as the only product of CO_2 reduction (Fig. 9C). The electrolyte did not contain other organic compounds, thus CO_2 was the only possible source of carbon for CH_3OH formation. The formation of methanol was confirmed by GC-MS (Fig. 9D), and its quantitative measurement was performed using the highly sensitive GC-BID technique. The obtained kinetic curves correspond to the observed density of photocurrents – with a decrease of the photoactivity of the material, producing both the lowering of the photocurrent density and flattening of the kinetic curve. The yield of methanol can be estimated, considering the amount of catalyst and non-continuous irradiation (3 s light and 4 s dark), at 56.7 μmol g^{-1} h^{-1}.

3.5. Studies under operation conditions

Cyclic voltammetry (CV) in the dark was measured in the range from 1 V *vs* RHE to 0 V and back to 1 V. While sweeping the potential, the electrode was oxidized or reduced, leading to changes of absorbance of material (directly observed by using the spectro-electrochemical setup shown in SI – Fig. S1). As shown in Fig. 10, voltammetry peaks correspond to the changes at ΔA curve. Going from a more positive potential to 0 V, the material seems to be stable and the absorbance of photocathode does not change significantly. Just small reduction peaks at CV curve between 0.3 and 0.1 V (zinc and copper reduction [50]) were observed. Strong cathodic peak at 0 V, in absence of CO_2, is related to the hydrogen evolution reaction and does not change the optical properties of the material. Opposite, an anodic scan (from 0 V to 1 V), resulted in a large decrease of the absorbance indicating the oxidation of CuO–ZnO. Anodic peak at +0.55 V *vs* RHE results from the copper oxidation (Cu^{I} to Cu^{II}) [50]. (*vide infra*).

To examine the elemental changes that take place during photocorrosion of the CuO–ZnO photocathode, we performed XAFS measurements on an area of photocathode that was PEC tested (for 24 h at 0.4 V *vs* RHE) and on the freshly prepared photocathode. Fig. 11A shows the X-ray absorption near edge spectroscopy (XANES) spectrum of the

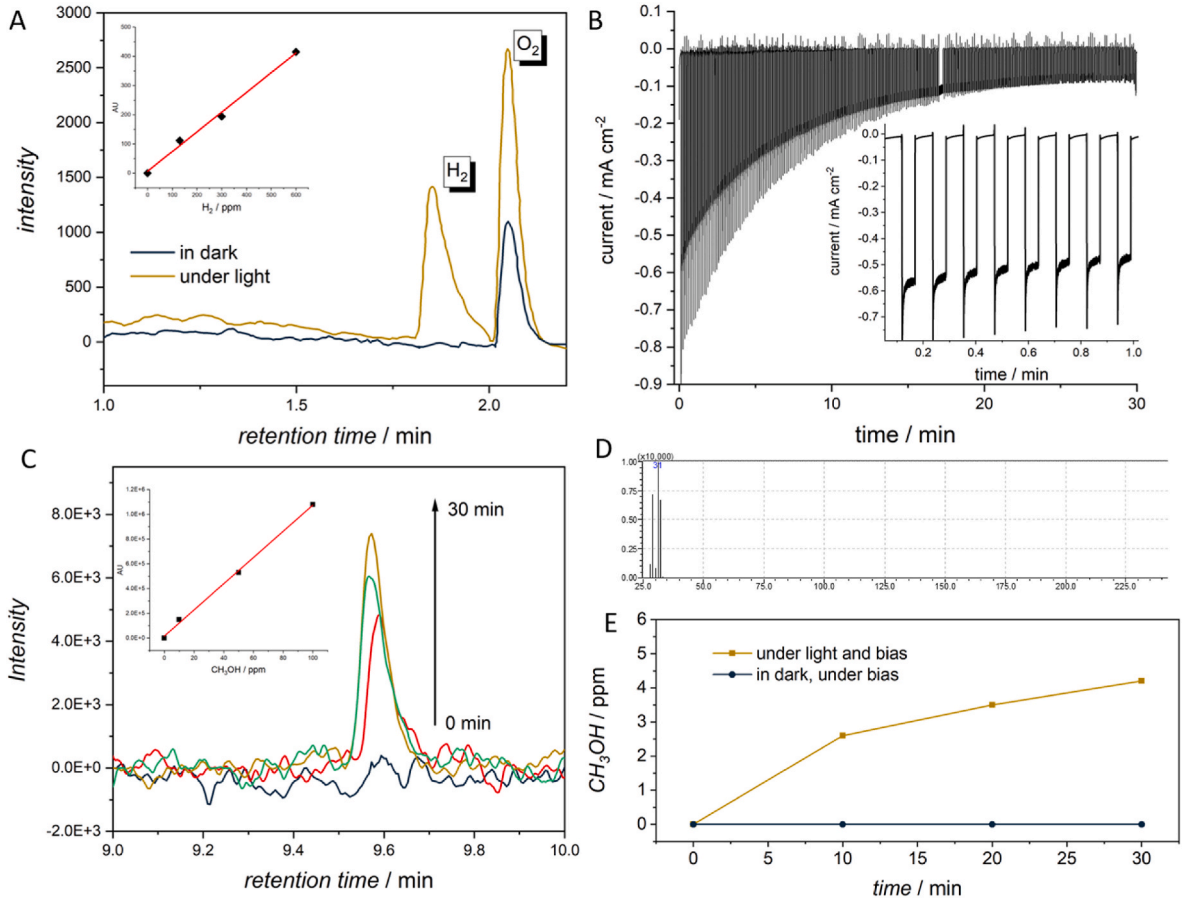

Fig. 9. Photoelectrochemical activity of CuO–ZnO. **A** – gas chromatograms of gas phase from above the cell with PEC in deoxygenated electrolyte (pH 7), inset – calibration curve for H_2 determination. **B** – chronoamperometric scan under chopped light, electrode biased at 0.55 V vs RHE. **C** – gas chromatograms of headspace of electrolyte during PEC test towards CO_2 reduction, inset – calibration curve for CH_3OH determination. **D** – MS spectrum (from GC-MS analysis) confirming the formation of CH_3OH. **E** – kinetic curves of PEC test using CuO–ZnO electrode and blank test performed in dark under bias at 0.55 V *vs* RHE.

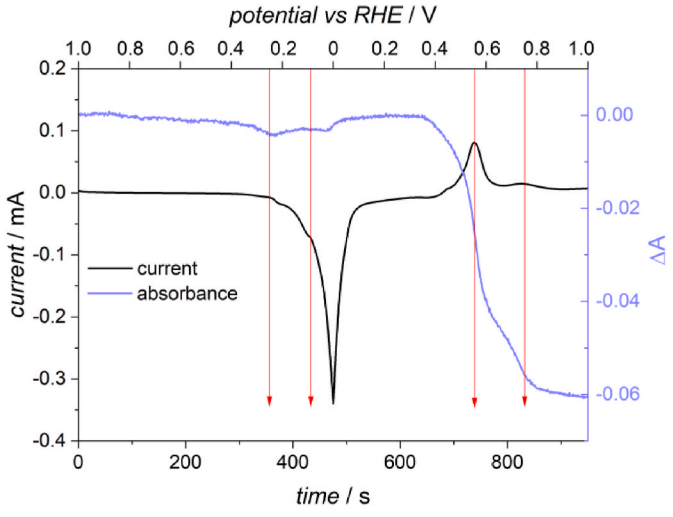

Fig. 10. Spectro-electrochemical measurements of CuO–ZnO in the dark. 0.1 M K_2HPO_4 + KH_2PO_4 (pH = 7) was used as an electrolyte. Black curve: cyclic voltammetry (left axis); blue curve: changes of absorbance in time during CV scan (right axis). (For interpretation of the references to color in this figure legend, the reader is referred to the Web version of this article.)

fresh film together with the respective spectrum of pure CuO. The two spectra show a perfect conformity, proving that the Cu in the fresh films is pure Cu^{II} oxide. The XANES of the used film (Fig. 11B) shows significant contributions of another Cu-species with Cu in lower oxidation state than +2, suggesting a reduction of copper in PEC conditions. The XANES region of the spectrum shows a linear combination of the spectra of pure CuO and Cu_2O (Fig. S8 in SI). A very good fit is achieved with a ratio of *ca.* 1:3 CuO to Cu_2O. Addition of the spectra of other species such as elemental Cu did not improve the fit.

Zn K-edge EXAFS were measured on two samples: a fresh and a used CuO–ZnO electrodes. Both samples were measured in total fluorescence yield mode using a PIPS diode. The fresh sample contains a significant amount of Zn. A comparison with the height of the Cu K-edge in the same sample suggests that the Zn content is about 3–5 times smaller than the Cu content. Noteworthy, in used samples the Zn-content was so low that an edge is hardly visible (Fig. 11C). Because of this low Zn-content no attempt was undertaken to measure the sample using an energy-dispersive detector. The height of the Zn K-edge in the spectra of the used films is minuscule indicating the almost complete loss of the Zn during the use of the electrodes. The Fourier transformed EXAFS spectrum (Fig. 11D) shows a first large peak at ~1.5 $Å^{-1}$. A peak at this position is typical for small atoms neighbours like oxygen. The second peak at ~2.8 Å-1 is probably caused by backscattering from a metal shell (probably Zn, but due to the very small differences between Zn and Cu, this backscattering could be also caused by Cu). The literature reports a close resemblance to Zn and Cu Fourier transformed EXAFS [51].

Flat band potentials were also determined *in operando* conditions based on the well-established method - open-circuit photovoltage

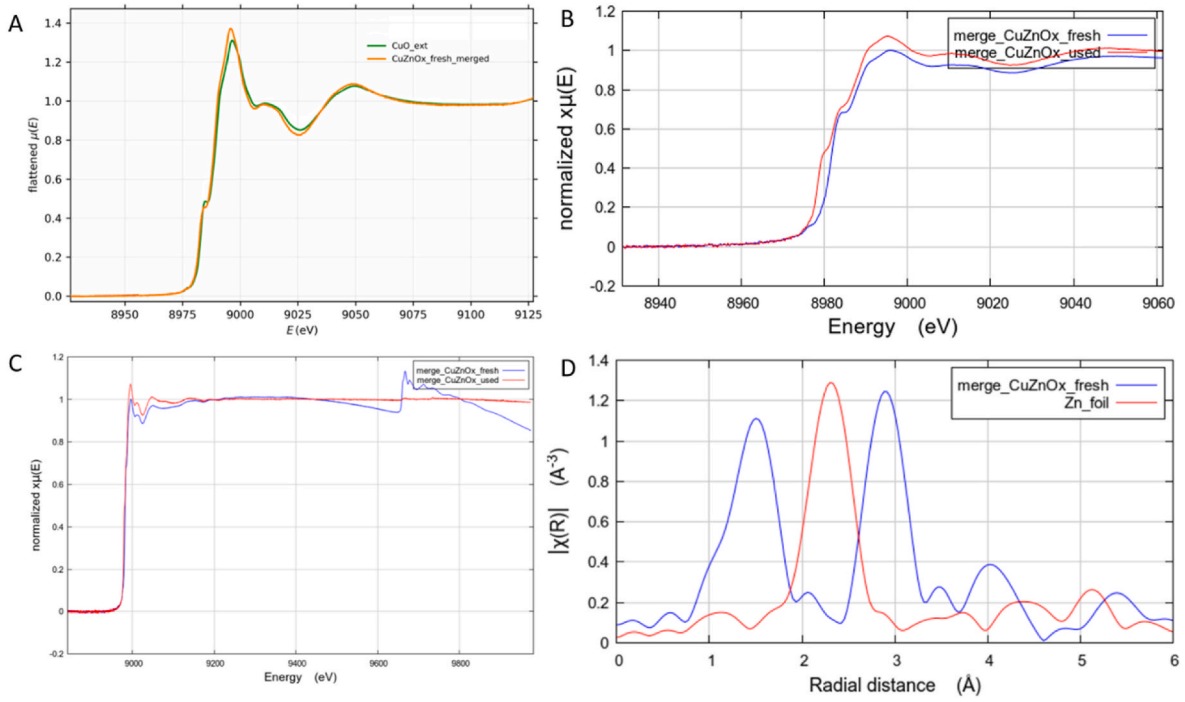

Fig. 11. X-ray absorption spectroscopy analysis. **A** – XANES spectrum of CuO–ZnO – Cu-edge together with standard of CuO. **B** – XANES analysis of the fresh and used CuO–ZnO – Cu-edge **C**- XANES analysis of the fresh and used CuO–ZnO films – Zn-edge. No Zn K-edge visible in the used film. The edges just before 9000 eV are the Cu K-edges. **D** - Fourier transformed EXAFS spectra of the fresh CuO–ZnO film and of a Zn foil. The spectrum of the film is the result of merging 10 spectra.

measurements [52]. After the contact of the semiconductor surface with the electrolyte, the Fermi level of the semiconductor E_F is adjusted to the Fermi level of the electrolyte $E_{F,redox}$ [53]. This process has the effect of charging the semiconductor, while the diffuse charge in the material is counterbalanced basically by a sheet of charge in the electrolyte [41]. External changing the voltage of the semiconductor results in the separation of E_F and $E_{F,redox}$, and hence the level of band bending due to electron depletion in the semiconductor depends on the applied voltage. If this external voltage is such that there is no band bending, the semiconductor is at its flat-band potential, V_{FB}, and there is no net transfer of charge. Under OCP conditions, the photogenerated holes are accumulating at semiconductor surface, which with increasing light intensity lowers the barrier for photogenerated electrons until the electrons can reach the surface at the same rate as holes. Simultaneously, the quasi-Fermi level increases due to the higher occupancy of the conduction band. The quasi-Fermi level can be measured as a OCP, which in case of high enough irradiation intensity (Fig. 12A), becomes constant and this value is very close to the potential of the valence band edge (for *p*-type semiconductor) [52,54]. Fig. 12B shows the measured open-circuit photovoltage of CuO–ZnO under increasing light intensity (each stair represents a 5% increase of relative intensity of light). Under illumination, the OCP shifts to a positive values. At pH = 7, with increase of the illumination intensity, the OCP approaches a limit of 0.45 V (Fig. 12C), and OCP becomes independent of intensity when the light intensity exceeds relative values of 70%. The determined E_{FB} was +1.07 V *vs* RHE (pH = 7). In case of measurements in sodium hydroxide electrolyte (pH 14) E_{FB} of was +0.89 V *vs* RHE, thus it does not follow the Nernst relation.

4. Discussion

The main goal of this work was to prepare a CuO–ZnO photoactive composite, in which a mutual charge transfer between oxides improves the efficiency and stability of the photocatalyst. As proved by XRPD and other techniques, the CuO–ZnO photomaterial described in this work shows a better contact between CuO and ZnO in comparison with mixed oxides or doped materials reported in the literature, that facilitates the charge transfer. The potential of conduction band of CuO (−3.66 eV respect to the vacuum [55]) lies higher in the energy scale in comparison with ZnO [56]. As a consequence, one can expect that, upon irradiation, photogenerated electrons from CB of CuO may migrate to CB of ZnO and subsequently towards the electrolyte, while holes move in the opposite direction, towards the biased support. However, the material here described does not correspond to the described model. Due to the strong interaction between CuO and ZnO proved by XRPD and the mutual co-doping, the composite imitates a single-phase material considering properties such as a band gap energy and flat band potential. The estimated energy of band gap of composite is 2.43 eV, which is lower than the band gap energy of bare ZnO (typically 3.2 eV [56]) and higher than that of neat CuO (reported in the range 1.2–1.8 eV [13]). Obtained DRS data suggest that the interfaces are combined closely and the band edges are matched well between these two semiconductors. Matching of band edges is not abnormal behavior and it was previously reported, for example in TiO_2/Cu_2O or CuO/g-C_3N_4 heterojunctions and many others [57,58]. In typical heterostructure, the crystals of one semiconductor grow on another one and the width of the transition region between these semiconductors is as little as a single atomic layer [59]. In parallel to matching of band structures the band bending in two semiconductors occurs, so that the Fermi level has the same value on both sides of semiconductor interface.

CuO–ZnO heterostructure was used as a photocathode in the water splitting reaction and CO_2 reduction. Upon irradiation the electrode generates photocurrents: under potentials lower than *ca.* 0.8 V a cathodic photocurrent (density up to 1.7 mA cm^{-2}) while under higher potentials, anodic photocurrents are generated. The switching potential corresponds to the flat band potential. Photocurrents are generated under irradiation by a broad range of light wavelength, from UV up to *ca.* 600 nm. Calculated Incident Photon to Current Efficiency is high and it reached the interesting value of 26%, with respect to 5 − 20 % for neat CuO [60,61], and 12% for CuO/ZnO [29,47,48], even if still lower than the value found for copper oxide covered with metallic platinum [12]. The measured cathodic photocurrents depend on the number of layers

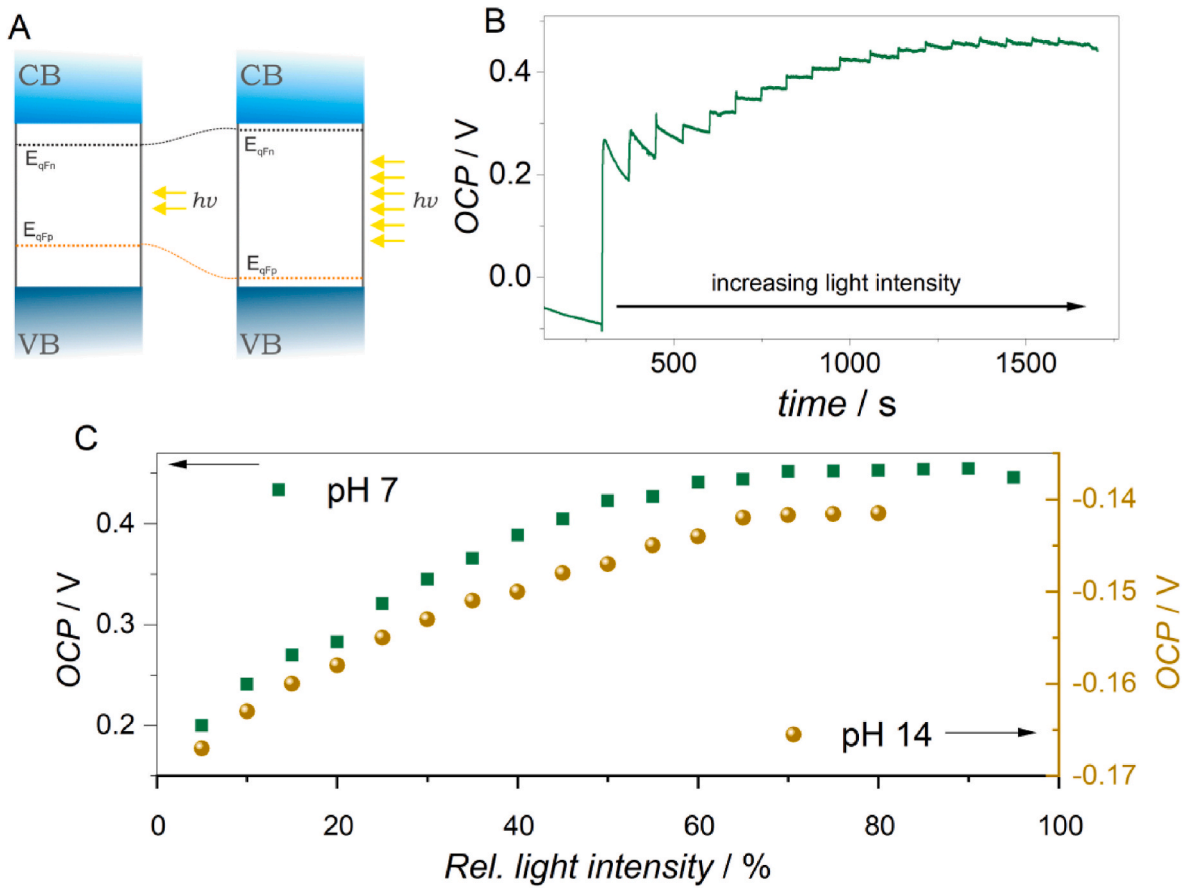

Fig. 12. Open-circuit photovoltage measurements. **A**- Fermi levels and quasi-Fermi levels of electrons for an *n*-type semiconductor and holes electrons for an *p*-type semiconductor under illumination – the number of yellow arrows indicates the intensity of light. **B**– OCP measurement of CuO–ZnO under an increasing light intensity (each stair represents a 5% increase of relative intensity of light) in a phosphate buffer pH = 7. Changes of OCP under an increasing light intensity in case of CuO–ZnO immersed in electrolyte at pH = 7 (squares plot, left axis) or pH = 14 (circles plot, right axis). (For interpretation of the references to color in this figure legend, the reader is referred to the Web version of this article.)

and the calcination temperature. The highest photocurrent density was observed in an alkaline solution in case of a photocathode composed of 4 layers of material annealed at 450 °C. Cathodic photocurrents are just slightly affected by the presence of sacrificial electron donor (methanol), proving a correct band potential for OER. PEC experiments performed in the deoxygenated electrolyte led to the formation of hydrogen at the surface of the photocathode. In turn, in presence of carbon dioxide (in aqueous solution as HCO_3^- at the operative pH) electrons from irradiated photocathode can drive the reduction of CO_2 to methanol.

In addition to high activity, the material also shows a relatively high stability. In long time chronoamperometric measurements, the efficiency of light conversion decreases during the first hour, and then the material reaches a nearly stationary condition because the photocurrent density does not change significantly over time up to 24 h. The reason of the decrease of light conversion efficiency was investigated by XAS measurements. Zn K-edge EXAFS measurement points at the leaching of zinc from the sample: after having been used for 24 h in PEC conditions the content of zinc is clearly reduced. The far-reaching changes of material was suggested also by spectro-electrochemical measurements, in which redox reactions of both copper and zinc species were discovered.

The activity of the materials produced in this work looks to be very promising and much improved with respect to similar systems described in the literature (Table 2). First of all, the density of generated photocurrents (*ca.* −1 mA/cm^2 as shown in Fig. 5A at applied bias 0.5 V vs RHE) is higher than that reported for neat CuO (*ca.* −0.4 mA/cm^2 [62]) even if somehow comparable with that of other ZnO/CuO composites [29,63,64]. With respect to the latter, our materials generate high photocurrents for at least 24 h, while described ZnO/Cu_2O–CuO composites show activity for not more than 12 h [25]. Regarding the CO2R, the literature reports examples of photocatalytic or photo-electrochemical systems based on copper or CuO/ZnO under a variety of experimental conditions. K.-L Bae has reported the concomitant production of methane and H_2 (1080 μmol·g_{cat}^{-1} h^{-1}) [65]. However, concerning the production of methanol the yield we have observed with our photo-materials (56.7 μmol g^{-1} h^{-1}) is significant even for the high

Table 2
Comparison of obtained results with literature data.

Material & conditions	H_2 evolution	CH_3OH production	References
CuO/ZnO without sacrificial electron donor	80 μmol h^{-1} g^{-1}	57 μmol h^{-1} g^{-1}	this study
ZnO/CuO supported in a zeolitic framework, synthesis involving organic compounds	62 μmol h^{-1} g^{-1}	–	Luévano-Hipólito et al. [27]
ZnO–ZnS/graphene photocatalyst in glycerol solution	1070 μmol h^{-1} g^{-1}	–	Chang et al. [68]
CuO@ZnO with the sacrificial electron donors	2353 μmol h^{-1} g^{-1}	–	Prabhu et al. [28]
Copper on graphene oxide, synthesis involving organic compounds		7 μmol g^{-1} h^{-1}	Shown et al. [67]
CuO/ZnO-embedded carbohydrate polymer	–	400 μmol g^{-1} h^{-1}	Belay Getahun et al. [66]

selectivity (no other C_1 products nor H_2 were formed) and certified for a record lifetime of *ca.* 24 h. A CuO/ZnO-embedded carbohydrate polymer film showed a yield of *ca.* 400 μmol g^{-1} h^{-1} [66] for only 3 h, while Shown et al. reported a yield of methanol of a few μmol·g^{-1}·h^{-1}, using copper oxide composites [67]. Please note that photosystems reported in Table 2 were tested in the presence of organic sacrificial electron donors, or materials were prepared in the presence of organic compounds, whose residuals can play a role as sacrificial agents.

To summarize, we have described in this paper a CuO–ZnO photocathode, in which a mutual-self-doping occurs. The photo-material shows a very high density of generated photocurrent, high IPCE value and a record 24+ h photoactivity. Photocathodes can be used for H_2 evolution in neat water or for reduction of CO_2 to methanol in presence of hydrogencarbonate anions, depending of the operative conditions. Interestingly, by using synchrotron techniques we have determined the reason of the gradual lowering of the photoactivity, that is represented by a slow leaching of zinc from the composite. The findings described in this paper from one side clarify the role of zinc in the composite (the mutual charge transfer) from the other help to better understand how the photo-materials work, which will allow to design more efficient photo-electrocatalysts.

CRediT authorship contribution statement

Tomasz Baran: Conceptualization, Investigation, Methodology, Validation, Visualization, Writing – original draft, Writing – review & editing. **Szymon Wojtyła:** Investigation, Methodology. **Marco Scavini:** Investigation, Methodology. **Francesco Carlà:** Investigation, Methodology. **Edmund Welter:** Investigation, Methodology. **Roberto Comparelli:** Investigation, Methodology. **Angela Dibenedetto:** Supervision, Writing – original draft, Writing – review & editing. **Michele Aresta:** Conceptualization, Methodology, Writing – original draft, Writing – review & editing.

Declaration of competing interest

The authors declare that they have no known competing financial interests or personal relationships that could have appeared to influence the work reported in this paper.

Data availability

No data was used for the research described in the article.

Acknowledgments

This work was financed by EU within Horizon Europe Research – DESIRED project (project code: 101083355). The authors acknowledge beamline ID03 at the European Synchrotron Radiation Facility and beamline P65 at the PETRA III facility in DESY Deutsches Elektronen-Synchrotron for providing beam time. Measurements in DESY (work order INDU-18-K09) was supported by the Baltic TRAM project, which is in part financed by the Interreg Baltic Sea Region Programme funded by the European Union.

Appendix A. Supplementary data

Supplementary data to this article can be found online at https://doi.org/10.1016/j.mtadv.2024.100477.

References

[1] P. Lianos, Appl. Catal. B Environ. 210 (2017) 235–254.
[2] G. Liu, N. Hoivik, K. Wang, H. Jakobsen, Sol. Energy Mater. Sol. Cells 105 (2012) 53–68.
[3] T. Baran, S. Wojtyła, A. Dibenedetto, M. Aresta, W. Macyk, ChemSusChem 9 (2016) 2933–2938.
[4] J. Highfield, Molecules 20 (2015) 6739–6793.
[5] M. Aresta, A. Dibenedetto, A. Angelini, Philos. Trans. R. Soc. Math. Phys. Eng. Sci. 371 (2013) 20120111.
[6] N. Fajrina, M. Tahir, Int. J. Hydrogen Energy 44 (2019) 540–577.
[7] T. Jafari, E. Moharreri, A.S. Amin, R. Miao, W. Song, S.L. Suib, Molecules 21 (2016) 900.
[8] A.K. Ringsmuth, M.J. Landsberg, B. Hankamer, Renew. Sustain. Energy Rev. 62 (2016) 134–163.
[9] S. Remiro-Buenamañana, H. García, ChemCatChem 11 (2019) 342–356.
[10] J. Prakash, S. Sun, H.C. Swart, R.K. Gupta, Appl. Mater. Today 11 (2018) 82–135.
[11] T. Baran, A. Visibile, S. Wojtyła, M. Marelli, S. Checchia, M. Scavini, F. Malara, A. Naldoni, A. Vertova, S. Rondinini, A. Minguzzi, Electrochim. Acta 266 (2018) 441–451.
[12] A. Paracchino, V. Laporte, K. Sivula, M. Grätzel, E. Thimsen, Nat. Mater. 10 (2011) 456–461.
[13] A.C. Cardiel, K.J. McDonald, K.-S. Choi, Langmuir 33 (2017) 9262–9270.
[14] H. Son, J.-H. Lee, P. Uthirakumar, D. Van Dao, A. Soon, I.-H. Lee, J. Alloys Compd. 942 (2023) 169094.
[15] H. son, J.-H. Lee, P. Uthirakumar, V. Dao, A. Soon, Y. Lee, I.-H. Lee, Nano Energy 117 (2023) 108904.
[16] P. Uthirakumar, Y. Lee, H. Son, V. Dao, C.Y. Kim, I.-H. Lee, J. Environ. Chem. Eng. 11 (2023) 111253.
[17] S. Jamali, A. Moshaii, N. Mohammadian, Phys. Status Solidi Appl. Mater. Sci. 214 (2017).
[18] S. Masudy-Panah, R. Siavash Moakhar, C.S. Chua, A. Kushwaha, G.K. Dalapati, ACS Appl. Mater. Interfaces 9 (2017) 27596–27606.
[19] A. Cots, P. Bonete, R. Gómez, ACS Appl. Mater. Interfaces 10 (2018) 26348–26356.
[20] T. Baran, S. Wojtyła, C. Lenardi, A. Vertova, P. Ghigna, E. Achilli, M. Fracchia, S. Rondinini, A. Minguzzi, ACS Appl. Mater. Interfaces 8 (2016) 21250–21260.
[21] X. Zhao, P. Wang, B. Li, Chem. Commun. 46 (2010) 6768–6770.
[22] D. Ren, J. Gao, L. Pan, Z. Wang, J. Luo, S.M. Zakeeruddin, A. Hagfeldt, M. Grätzel, Angew. Chem. Int. Ed. 58 (2019) 15036–15040.
[23] A. Kargar, Y. Jing, S.J. Kim, C.T. Riley, X. Pan, D. Wang, ACS Nano 7 (2013) 11112–11120.
[24] C. Liu, F. Meng, L. Zhang, D. Zhang, S. Wei, K. Qi, J. Fan, H. Zhang, X. Cui, Appl. Surf. Sci. 469 (2019) 276–282.
[25] H. Yoo, S. Kahng, J. Hyeun Kim, Sol. Energy Mater. Sol. Cells 204 (2020) 110211.
[26] T.P. Yendrapati Taraka, A. Gautam, S.L. Jain, S. Bojja, U. Pal, J. CO2 Util. 31 (2019) 207–214.
[27] E. Luévano-Hipólito, L.M. Torres-Martínez, A. Fernández-Trujillo, J. Phys. Chem. Solid. 151 (2021) 109917.
[28] Y.T. Prabhu, V.N. Rao, M.V. Shankar, B. Sreedhar, U. Pal, New J. Chem. 43 (2019) 6794–6805.
[29] K. Zhang, W.-F. Cai, J.-W. Shi, Q.-Y. Chen, J. Chem. Technol. Biotechnol. 97 (2022) 914–923.
[30] L. Zhang, D. Jing, L. Guo, X. Yao, ACS Sustain. Chem. Eng. 2 (2014) 1446–1452.
[31] S. Wojtyła, T. Baran, Int. J. Hydrogen Energy 44 (2019) 27343–27353.
[32] C. Ponchut, J.M. Rigal, J. Clément, E. Papillon, A. Homs, S. Petitdemange, J. Instrum. 6 (2011) C01069. C01069.
[33] S. Roobol, W. Onderwaater, J. Drnec, R. Felici, J. Frenken, J. Appl. Crystallogr. 48 (2015) 1324–1329.
[34] M.E. Orazem, B. Tribollet, V. Vivier, S. Marcelin, N. Pébère, A.L. Bunge, E.A. White, D.P. Riemer, I. Frateur, M. Musiani, ECS Trans. 45 (2013) 15–35.
[35] R.D. Shannon, Acta Crystallogr. A 32 (1976) 751–767.
[36] K. Joshi, M. Rawat, S.K. Gautam, R.G. Singh, R.C. Ramola, F. Singh, J. Alloys Compd. 680 (2016) 252–258.
[37] R.W.G. Wyckoff, Crystal Structures, second ed., Interscience Publishers, New York, 1963.
[38] J. Albertsson, S.C. Abrahams, Å. Kvick, Acta Crystallogr. B 45 (1989) 34–40.
[39] S.V. Bhosale, M. Al Kobaisi, R.W. Jadhav, L.A. Jones, Chem. Rec. 21 (2021) 257–283.
[40] N. Parveen, M.H. Cho, Sci. Rep. 6 (2016) 27318.
[41] K. Gelderman, L. Lee, S.W. Donne, J. Chem. Educ. 84 (2007) 685.
[42] S. Wojtyła, T. Baran, J. Inorg. Organomet. Polym. Mater. 27 (2017) 436–445.
[43] K.R. Reyes-Gil, E.A. Reyes-García, D. Raftery, J. Electrochem. Soc. 153 (2006) A1296–A1301.
[44] M. Anderman, J.H. Kennedy, J. Electrochem. Soc. 131 (1984) 21–26.
[45] Y. Takahashi, M. Jeem, L. Zhang, S. Watanabe, Appl. Mater. Today 26 (2022) 101359.
[46] C. Ma, Z. Liu, Z. Tong, C. Han, Q. Cai, Appl. Phys. 125 (2019) 451.
[47] A.A. Dubale, C.-J. Pan, A.G. Tamirat, H.-M. Chen, W.-N. Su, C.-H. Chen, J. Rick, D. W. Ayele, B.A. Aragaw, J.-F. Lee, Y.-W. Yang, B.-J. Hwang, J. Mater. Chem. A 3 (2015) 12482–12499.
[48] G. Panzeri, M. Cristina, M.S. Jagadeesh, G. Bussetti, L. Magagnin, Sci. Rep. 10 (2020) 18730.
[49] S.P. Berglund, F.F. Abdi, P. Bogdanoff, A. Chemseddine, D. Friedrich, R. van de Krol, Chem. Mater. 28 (2016) 4231–4242.
[50] G. Milazzo, S. Caroli, V.K. Sharma, Tables of Standard Electrode Potentials, Wiley, Chichester, 1977.
[51] A. Patlolla, J. Zunino, A.I. Frenkel, Z. Iqbal, J. Mater. Chem. 22 (2012) 7028–7035.
[52] R. Beranek, Adv. Phys. Chem. 2011 (2011) e786759.
[53] M.X. Tan, P.E. Laibinis, S.T. Nguyen, J.M. Kesselman, C.E. Stanton, N.S. Lewis, in: K.D. Karlin (Ed.), Prog. Inorg. Chem., John Wiley & Sons, Inc, 1994, pp. 21–144.
[54] Y.V. Pleskov, V.M. Mazin, Y.E. Evstefeeva, V.P. Varnin, I.G. Teremetskaya, V. A. Laptev, Electrochem. Solid State Lett. 3 (2000) 141–143.

[55] C.-Y. Chiang, Y. Shin, K. Aroh, S. Ehrman, Int. J. Hydrogen Energy 37 (2012) 8232–8239.
[56] A. Hamrouni, N. Moussa, F. Parrino, A. Di Paola, A. Houas, L. Palmisano, J. Mol. Catal. Chem. 390 (2014) 133–141.
[57] Y. Wang, J. Tao, X. Wang, Z. Wang, M. Zhang, G. He, Z. Sun, Ceram. Int. 43 (2017) 4866–4872.
[58] S. Wojtyła, K. Szmit, T. Baran, J. Inorg. Organomet. Polym. Mater. 28 (2018) 492–499.
[59] H. Ibach, H. Lüth, Solid-State Phys, Springer Berlin Heidelberg, Berlin, Heidelberg, 1991.
[60] Y.J. Jang, J.-W. Jang, S.H. Choi, J.Y. Kim, J.H. Kim, D.H. Youn, W.Y. Kim, S. Han, J. Sung Lee, Nanoscale 7 (2015) 7624–7631.
[61] H. Uchiyama, K. Isobe, H. Kozuka, RSC Adv. 7 (2017) 18014–18018.
[62] Y. Yang, D. Xu, Q. Wu, P. Diao, Sci. Rep. 6 (2016) 35158.
[63] U. Shaislamov, H.-J. Lee, J. Kor. Phys. Soc. 69 (2016) 1242–1246.
[64] N. Bahnasawy, A.M. Elbanna, M. Ramadan, N.K. Allam, Sci. Rep. 12 (2022) 16785.
[65] K.-L. Bae, J. Kim, C.K. Lim, K.M. Nam, H. Song, Nat. Commun. 8 (2017) 1156.
[66] M. Belay Getahun, E. Budi Santiko, T. Imae, C.-L. Chiang, Y.-G. Lin, Appl. Surf. Sci. 604 (2022) 154515.
[67] I. Shown, H.-C. Hsu, Y.-C. Chang, C.-H. Lin, P.K. Roy, A. Ganguly, C.-H. Wang, J.-K. Chang, C.-I. Wu, L.-C. Chen, K.-H. Chen, Nano Lett. 14 (2014) 6097–6103.
[68] C.-J. Chang, Y.-G. Lin, H.-T. Weng, Y.-H. Wei, Appl. Surf. Sci. 451 (2018) 198–206.